

# In Vivo Imaging of Newt Lens Regeneration: Novel Insights Into the Regeneration Process

Weihao Chen<sup>1,\*</sup>, Georgios Tsissios<sup>2-4,\*</sup>, Anthony Sallèse<sup>2,3</sup>, Byran Smucker<sup>3,5</sup>, Anh-Thu Nguyen<sup>1</sup>, Junfan Chen<sup>6</sup>, Hui Wang<sup>1,3</sup>, and Katia Del Rio-Tsonis<sup>2-4</sup>

<sup>1</sup> Department of Chemical, Paper and Biomedical Engineering, Miami University, Oxford, OH, USA

<sup>2</sup> Department of Biology Miami University, Oxford, OH, USA

<sup>3</sup> Center for Visual Sciences at Miami University, Oxford, OH, USA

<sup>4</sup> Cellular Molecular and Structural Biology Program, Miami University, Oxford, OH, USA

<sup>5</sup> Department of Statistics, Miami University, Oxford, OH, USA

<sup>6</sup> Department of Chemistry and Biochemistry, Miami University, Oxford OH, USA

**Correspondence:** Katia Del Rio-Tsonis, Department of Biology and Center for Visual Sciences, Miami University, 700 East High Street, 244 Pearson Hall, Oxford, OH 45056, USA. e-mail: [delriok@miamioh.edu](mailto:delriok@miamioh.edu)

Hui Wang, Department of Chemical, Paper and Biomedical Engineering, 64 Engineering Building, 650 East High Street, Oxford, OH 45056, USA. e-mail: [hui.wang@miamioh.edu](mailto:hui.wang@miamioh.edu)

**Received:** January 31, 2021

**Accepted:** March 28, 2021

**Published:** August 12, 2021

**Keywords:** OCT; lens regeneration; newt; iris; transdifferentiation

**Citation:** Chen W, Tsissios G, Sallèse A, Smucker B, Nguyen A-T, Chen J, Wang H, Del Rio-Tsonis K. In vivo imaging of newt lens regeneration: Novel insights into the regeneration process. *Transl Vis Sci Technol.* 2021;10(10):4.

<https://doi.org/10.1167/tvst.10.10.4>

**Purpose:** To establish optical coherence tomography (OCT) as an *in vivo* imaging modality for investigating the process of newt lens regeneration.

**Methods:** Spectral-domain OCT was employed for *in vivo* imaging of the newt lens regeneration process. A total of 37 newts were lentectomized and followed by OCT imaging over the course of 60 to 80 days. Histological images were obtained at several time points to compare with the corresponding OCT images. Volume measurements were also acquired.

**Results:** OCT can identify the key features observed in corresponding histological images based on the scattering differences from various eye tissues, such as the cornea, intact and regenerated lens, and the iris. Lens volume measurements from three-dimensional OCT images showed that the regenerating lens size increased linearly until 60 days post-lentectomy.

**Conclusions:** Using OCT imaging, we were able to track the entire process of newt lens regeneration *in vivo* for the first time. Three-dimensional OCT images allowed us to volumetrically quantify and visualize the dynamic spatial relationships between tissues during the regeneration process. Our results establish OCT as an *in vivo* imaging modality to track/analyze the entire lens regeneration process from the same animal.

**Translational Relevance:** Lens regeneration in newts represents a unique example of vertebrate tissue plasticity. Investigating the cellular and morphological events that govern this extraordinary process *in vivo* will advance our understanding and shed light on developing new therapies to treat blinding disorders in higher vertebrates.

## Introduction

Regenerative medicine provides great hope for treating ocular pathologies and overcoming irreversible vision loss. Amphibians such as frogs, axolotls, and newts are the closest relatives to humans that can regenerate a full lens after injury or complete lens removal including the lens capsule. Frogs lose this ability after metamorphosis and axolotls after embryonic devel-

opment.<sup>1-5</sup> Newts, however, retain full lens regenerative capabilities throughout their entire lifespan.<sup>5</sup> Even more astonishing, lens regeneration in newts is not altered by age or repetitive damage,<sup>6,7</sup> thereby providing a model to study preventative or treatment strategies for age-related ophthalmic disorders in higher vertebrates.

Our current understanding of the cellular mechanisms during lens regeneration in newts mainly comes from studies employing acquisition techniques such as

transmission and scanning electron microscopy, light microscopy with hematoxylin–eosin (H&E) staining and in situ hybridization, transmission scatter measuring system analysis, and immunofluorescence.<sup>8–15</sup> Although the use of these technologies has expanded our understanding of the process of newt lens regeneration in the past decades, these are all *ex vivo* imaging technologies, and most of them require extensive tissue processing. These technologies can only assess morphological or cellular changes at a fixed point in time. Therefore, tracking the entire process of lens regeneration requires the sacrifice of many animals at different time points. This results in lost continuity of the lens regeneration process and a failure to capture the complex and dynamic spatiotemporal tissue remodeling that occurs during lens regeneration. Here, we describe an *in vivo* imaging modality that eliminates the need to sacrifice large cohorts of animals and provides new insights into the dynamic cellular mechanisms that have remained undetected or masked by *ex vivo* technologies.

Optical coherence tomography (OCT) is a real-time non-invasive tissue imaging modality that can acquire cross-sectional images, similar to histology, by measuring the backscattered light echoes from tissues.<sup>16</sup> Since its introduction in 1991, OCT has been established as an imaging technology routinely used in ophthalmology.<sup>17–19</sup> OCT has also been widely adopted in ophthalmologic research in small animals.<sup>20–23</sup> Several regenerative studies in zebrafish, rat, and planaria have taken advantage of OCT to examine dynamic changes during the regeneration process.<sup>24–27</sup> Here, we establish OCT as an *in vivo* imaging modality to track the entire process of newt lens regeneration, using histological images as a reference, and to obtain volumetric measurements of the regenerating lens as a function of time.

## Methods

### Animal Procedures and Ethics Statement

Red spotted newts, *Notophthalmus viridescens*, were obtained from Bald Mountain Gardens (Boston, MA). All procedures were performed according to the guidelines approved by the Institutional Animal Care and Use Committee at Miami University and the ARVO Statement for the Use of Animals in Ophthalmic and Vision Research. Before any surgery or imaging, animals were anesthetized by immersion in 0.1% ethyl 3-aminobenzoate-methane sulfonic acid solution (MS222) prepared in amphibian phosphate-buffered

saline. Lens removal (lentectomy) was achieved by making an incision through the cornea with a scalpel and then carefully removing the entire lens with tweezers.<sup>28</sup> Lentectomies were performed in both eyes of the animals. All animals were monitored until they recovered from anesthesia and were then returned to their cages. During the study, animals were monitored and kept under the recommended husbandry conditions.<sup>29</sup>

### Spectral-Domain OCT

A spectral-domain OCT device, developed at Miami University, was employed for all of the studies. This device uses a supercontinuum light source (YSL Photonics, Wuhan City, China) filtered at  $\sim 800$  nm, with  $\sim 150$  nm full width at half maximum as a broadband light source for these studies. The output power in the sample arm was  $\sim 2.3$  mW. The images were acquired at 17 frames/s with 20,000 A-scans per second. For each newt, the OCT instrument scanned an area  $1.2$  mm  $\times$   $1.2$  mm over the anterior eye surface with 1000 A-scans per B-scan and 1000 B-scans per C-scan. The axial resolution was  $\sim 2$   $\mu$ m, and the lateral resolution was  $\sim 7.9$   $\mu$ m. To resolve the complex conjugate ambiguity associated with spectral-domain OCT, an  $\sim 2$ -mm offset was introduced relative to the pivot point of the scanner to generate Doppler frequency shifts.<sup>30</sup> A five-dimensional translational stage with an adapter was used to stably hold the newts during imaging, as shown in Figure 1.

### Live Imaging and Histology

A total of 37 animals were used in two independent experiments. The first experiment compared OCT images with the histological images acquired at different stages of lens regeneration. Immediately after OCT imaging, animals were euthanized and whole eyes were surgically removed from the orbit by cutting the optic nerve. The eyes were subsequently fixed and processed for histology. We chose 12 different time points to compare OCT images with histological images. The time points included intact eyes and eyes collected at 4, 8, 12, 16, 22, 30, 34, 40, 45, 52, and 80 days post-lentectomy (dpl). As indicated from previous studies, these time points represent important stages during newt lens regeneration.<sup>10–12,31–35</sup>

The sample size per time point was three animals (six eyes), resulting in a total of 36 animals (72 eyes). Although only 12 time points were collected for histology, OCT imaging was conducted for additional time points, including 0, 2, 10, 14, 18, 20, 24, 26, 28, 32, 36, 38, 43, 48, 50, 55, 60, 65, and 75 dpl, for which

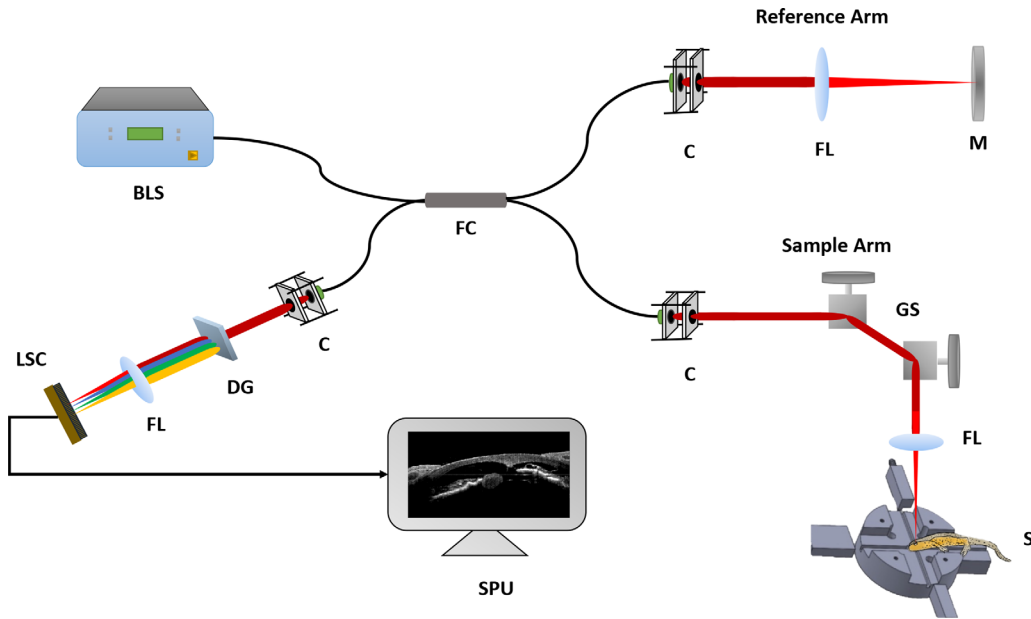


**Figure 1.** Spectral-domain OCT imaging platform setup. The board band light source (BLS) has a total of 20 mW of power output and a frequency of 200 MHz. About 20% light is coupled into the fiber-based spectral-domain OCT system. The fiber coupler (FC) splits the input light by 50/50 into a reference arm and a sample arm. The average power rate at the sample arm is about 2.3 mW. Polarization is optimized to maximize the imaging depth. A 2-mm offset is introduced at the first galvanometer scanning mirror from the pivot point, so that the mirror artifact can be resolved by Hilbert transformation. A line scanning camera (LSC) captures coherence signals with 27,000 A-scans per second, resulting in a display at 17 frames/s. The signal processing unit (SPU) includes an image and acquisition card, a digital analog card, and a computer. These components transfer, process, and display the OCT data. PC, polarization controller; FL, focusing lens; C, collimator; GS, galvanometer scanner; M, mirror; DG, diffractive grating.

corresponding H&E images were not performed. The second experiment utilized OCT to continuously track lens regeneration from the same eye of an individual newt for 60 days, with images taken from the intact eye and at 0, 5, 8, 11, 18, 21, 25, 28, 32, 39, 42, 49, 53, and 60 dpl.

For histology, whole eye tissues were fixed in 4% paraformaldehyde overnight at 4°C and either cryoprotected in 30% sucrose prior to cryo-embedding or processed for paraffin embedding. For cryosectioning, eyes were cut at a 20- $\mu\text{m}$  thickness, whereas for paraffin embedding they were cut at 10  $\mu\text{m}$ . Serial sections were collected from the entire area of the pupillary margin of the iris and processed for standard H&E staining. All histological procedures were performed as described previously.<sup>28</sup>

## Image Processing and Reconstruction

The imaging processing pipeline was customized and implemented with MATLAB (R2019a version; MathWorks, Natick, MA). The processing sequence included noise subtraction, wavenumber recalibration, Hilbert transformation, Fourier transformation, complex modulus calculation, and log compression for displaying. The imaging depth of B-scans

was calibrated with a  $170 \pm 5\text{-}\mu\text{m}$  microscopy cover glass (Deckgläser; Waldemar Knittel Glasbearbeitungs, Braunschweig, Germany). The tissue refractive index was assumed to be 1.38. All three-dimensional (3D) images were reconstructed by stacking B-scans in series using ImageJ (National Institutes of Health, Bethesda, MD) into a  $500 \times 500 \times 500$ -pixel volume. Then, the scale of this volume was corrected by matching the 1:1 ratio of the rectangular scanning area (1.2 mm  $\times$  1.2mm). A B-scan closest to the histological section position was chosen at various stages to compare with the corresponding histological images.

## Segmentation and Pseudocolor

Different tissues, including the cornea, iris, and lens, were first manually segmented on the B-scans using the Segmentation Editor plugin from ImageJ. Depending on the irregularity of different tissues, 10 to 50 slices were manually segmented as the baseline for each tissue, then the rest of the interval slices were unraveled using the interpolation function from ImageJ. With the original C-scan data representing the gray channel, each tissue type was labeled with a pseudocolor and merged into a four-channel stack. These 3D four-channel images are visualized and

Results

Comparing OCT Images With Histological Images at Different Days Post-Lentectomy

To explore the capability of *in vivo* OCT imaging in live newts, we compared OCT images with the corresponding H&E stained histological images at representative days post-lentectomy, as shown in Figure 3. A graphical illustration (Fig. 3, right column) is used to aid visualization of morphological changes during regeneration. OCT images are depicted in grayscale (Fig. 3, left column), where different tissues can be recognized based on backscattering properties (higher backscattering = brighter signal). The H&E stained sections are shown in conventional RGB color images (Fig. 3, center column). Figures 3A and A' shows OCT and H&E images of the intact anterior chamber of a newt eye. The cornea, a multilayer tissue that consists of stratified epithelial cell layers at the anterior surface, a collagen-filled stroma in the middle, and an endothelial layer at the posterior surface, is clearly visible.<sup>36</sup> The brightest signal observed in the OCT images of the newt eyes comes from the pigmented epithelial cells (PECs) of the dorsal and ventral iris (Di and Vi, respectively). These cells are heavily packed with melanin pigments whose function is to absorb light, resulting in high light backscattering, shown as the bright signal in the OCT images.<sup>36–38</sup> A thin stroma layer composed of collagen fibrils, blood vessels, contractile muscles, and melanocytes can be visualized on top of the iris PECs (iPECs).<sup>39</sup> In the pupil area, between the Di and the Vi, the fully developed adult intact lens can be seen with weak scattering in the OCT images. The lens consists of an anterior layer of lens epithelium (LE) and lens fibers (LFs).<sup>36</sup> Differences in organelle composition between primary lens fibers (1°LFs) in the lens nucleus and secondary lens fibers (2°LFs) in the lens cortex can be seen in the inset image in Figure 3A with enhanced contrast.<sup>40–42</sup> Tissue fixation and histological processing often result in damage to the fragile lens fibers (Fig. 3A'), but these are well represented in the OCT image (Fig. 3A). Tissues below the iris, including the zonule fibers and the ciliary body, are not visible in the OCT image, as the light is blocked by the iris.

Figures 3B to F show representative OCT images, histological images, and graphical illustrations of the lens regeneration process at 8, 16, 22, 34, and 80 dpl. Additional time points are shown in Supplementary Figure S1. At 8 dpl, the cornea incision caused by the lentectomy was partially healed, which was evident in the OCT image (Fig. 3B), as well as the H&E image

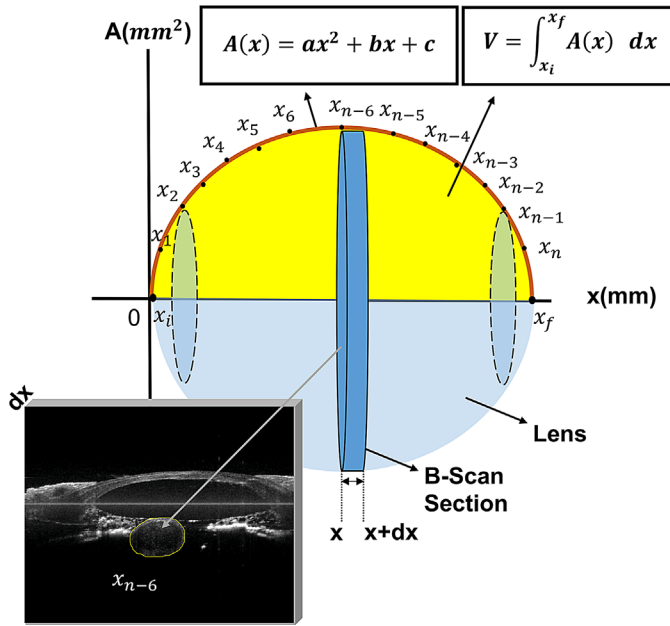


**Figure 2.** Lens volume quantification methodology:  $A(x)$  is shown as the orange curve, which is the quadratic relationship between the lens cross-sectional area  $A$  and its corresponding location at  $x$ . This quadratic curve is obtained by fitting a series of lens cross-section areas measured from B-scans. An example of a 30-dpl lens cross-section area measurement at location  $x_{n-6}$  is shown. The roots of this quadratic equation were assigned as  $x_i$  to  $x_f$ , which represent the initial and final positions, respectively. The volume is the integral of  $A(x)$  from  $x_i$  to  $x_f$ , and it is also the area under the quadratic curve, which is shown as the yellow area.

animated using ICY software (Institut Pasteur, Paris, France; France BioImaging, Montpellier, France), and Imaris Viewer (Oxford Instruments, Abingdon, UK).

Quantitative Analysis of Lens Size

As OCT can acquire 3D images of the regenerated lens, the volume of the lens was quantified at different days post-lentectomy. Fifty to 150 B-scans containing the lens were chosen and then manually segmented from each B-scan to calculate the cross-sectional area, defined as  $A(x_1)$ ,  $A(x_2)$ , ...,  $A(x_n)$ . The analytical form of  $A(x)$  can be obtained by fitting  $A(x_1)$ ,  $A(x_2)$ , ...,  $A(x_n)$ , with a quadratic equation. The volume of a lens was calculated by integrating  $A(x)$  from  $x_i$  to  $x_f$ , which are the initial and final positions, respectively, of a lens along the C-scan direction and were calculated as the roots of  $A(x)$ . In addition, the relationship between the volume of the lens and the time after lentectomy, defined as  $V(t)$ , was fitted with a quadratic equation. Figure 2 depicts the methodology for quantifying each lens volume from OCT images.

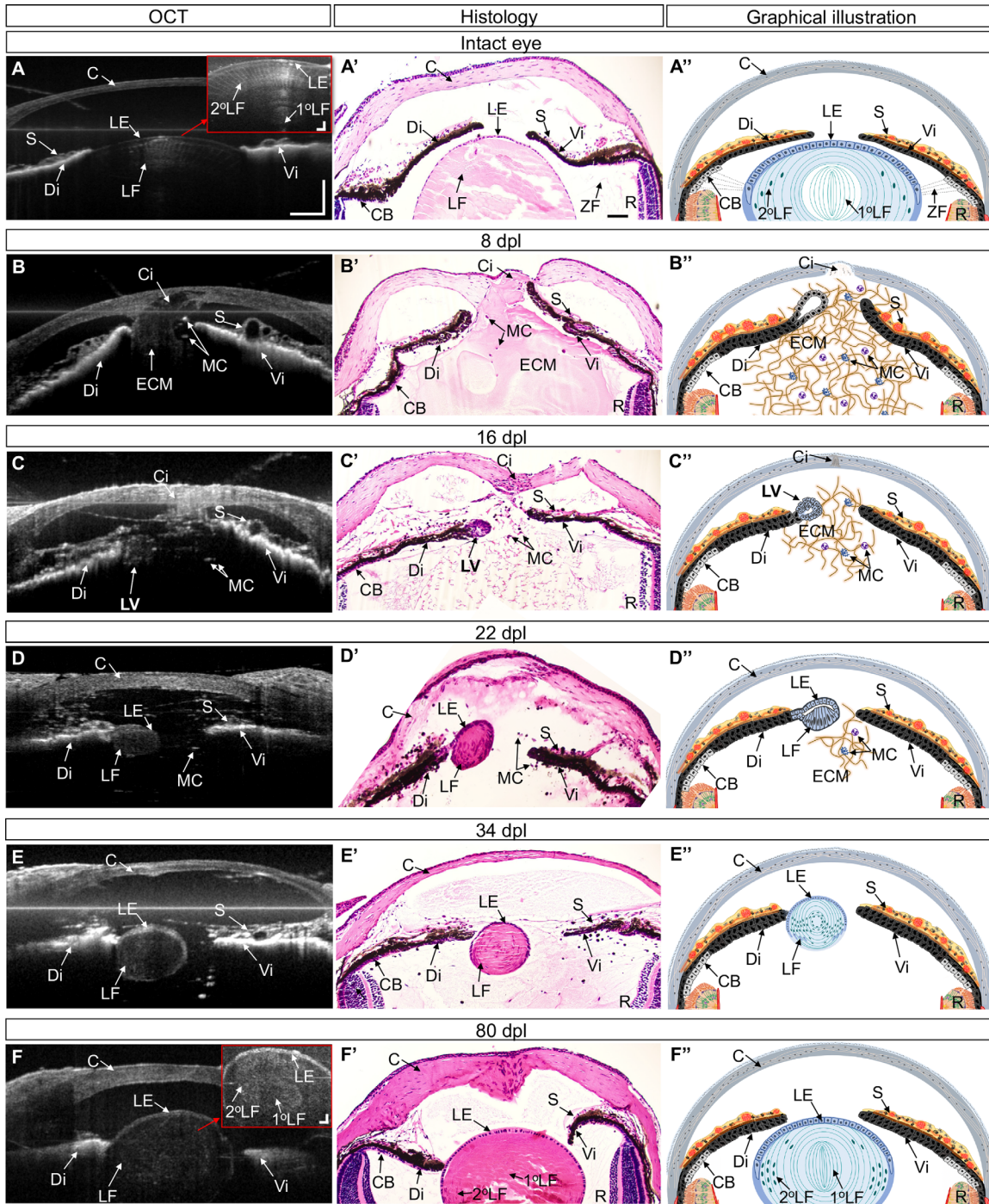


**Figure 3.** Medial sagittal sections of the anterior segment of the intact and regenerated adult newt eye as depicted by OCT (left column), H&E (middle column), and graphical illustration (right column). The eye orientation is kept the same in all images with the dorsal iris (Di) on the left and ventral iris (Vi) on the right. In the intact eye, the aqueous chamber is clear, and the iris shows strong scattering. The inset image in A shows fine morphology, with the lens fibers arranged in a series of concentric spherical shells and a distinct nucleus (**A, A', A''**). At 8 dpl the iris becomes thicker, and the aqueous chamber is filled with extracellular matrix (ECM) (**B, B', B''**). At 16 dpl, an early lens vesicle (LV) is present at the pupillary margin of the dorsal iris (**C, C', C''**). The lens vesicle grows in size and there are signs of lens fiber differentiation at 22 dpl (**D, D', D''**). At 34 dpl the lens epithelium (LE) in the anterior part of the regenerating lens covers a mass of differentiating lens fibers (LFs) (**E, E', E''**). At 80 dpl, the lens appears more mature and compact. (**F**) The inset image shows the lens at higher magnification and contrast to facilitate visualization of 1° and 2°LFs; the corresponding H&E and graphical illustration of this time point can be seen in **F'** and **F''**. Scale bars: 100 μm in A, which applies to all OCT images; 25 μm in inset images in A and F; 100 μm in A', which applies to all H&E images. C, cornea; Ci, cornea incision; S, stroma; 1°LF, primary lens fiber; 2°LF, secondary lens fiber; MC, migrating cell; ZF, zonule fiber; CB, ciliary body; R, retina.

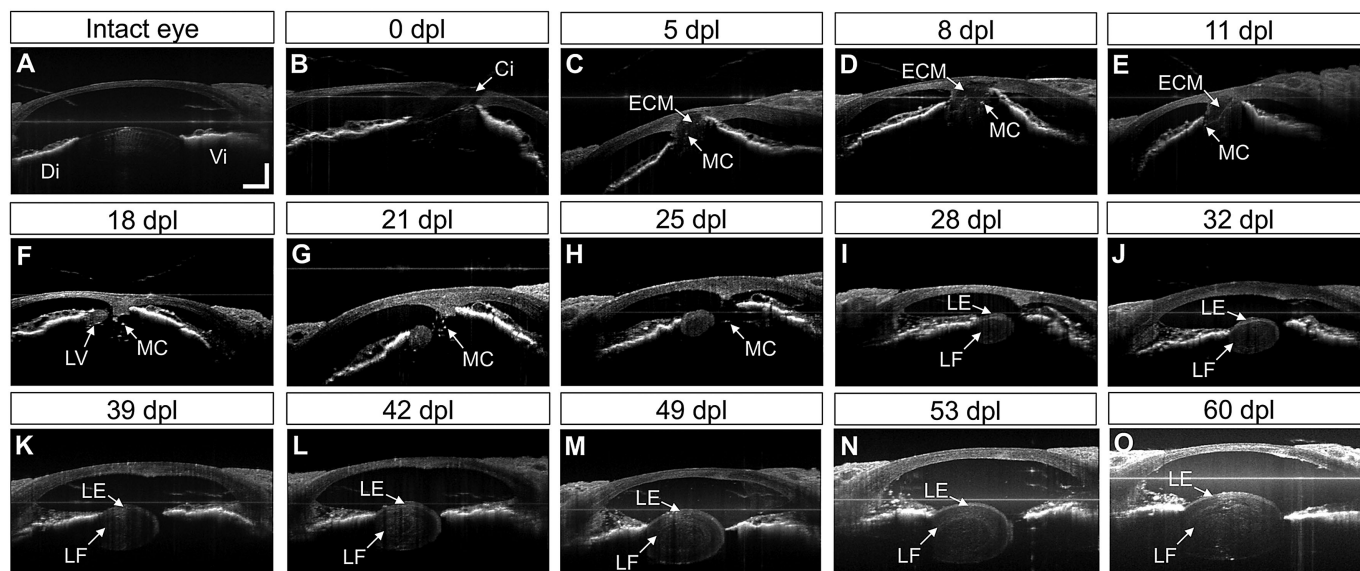


**Figure 4.** OCT images of an individual newt eye undergoing lens regeneration. OCT imaging series start with the intact eye (A) followed by lentectomized eyes from 0–60 (B–O) dpl. The eye orientation is kept the same in all images with dorsal iris (Di) on the left and ventral iris (Vi) on the right. Scale bars: 100  $\mu\text{m}$  in A, which applies to all images. The contrast in the 60-dpl image was enhanced to visualize the entire lens.

(Fig. 3B'). In an intact eye, the aqueous chamber is clear, allowing light to pass through the lens (Fig. 3A). However, after lentectomy, the aqueous chamber fills with extracellular matrix (ECM).<sup>32</sup> Accumulation of the ECM in the aqueous chamber can be observed in the H&E image (Fig. 3B') and with weak scattering via OCT (Fig. 3B). Aggregation of migrating cells can be detected along with the ECM in the H&E image and appears as bright spots in the OCT image (Figs. 3B, B'). The dilation of the blood vessels in the stroma is also visible in the OCT image (Fig. 3B). The increase in iris thickness can be observed by comparing the iris epithelium in both OCT and H&E images between intact and 8 dpl (Figs. 3A, B). At 16 dpl (Fig. 3C), the cornea is almost healed, and a lens vesicle is observed at the pupillary margin of the Di in both the OCT and the H&E images (Figs. 3C, C'). Compared with the iPECs, the transdifferentiated cells in the lens vesicle show less scattering contrast in the OCT image, indicating that iPECs have undergone depigmentation. By 22 dpl (Fig. 3D), the regenerated lens on the Di can be observed. The cells at the posterior surface of the lens vesicle elongate and differentiate into LFs, giving rise to an early regenerated lens (Fig. 3D'). The LE becomes visible in the OCT image as a thin layer with relatively stronger scattering contrast compared with that from the LFs (Fig. 3D). At this point, the cornea has fully healed. From this stage forward, the growth pattern of the regenerated lens mimics normal vertebrate lens development in terms of sequential morpho-

logical events and crystallin accumulation.<sup>43</sup> At 34 dpl, the regenerating lens increases in size and LF content (Figs. 3E, E'). By 80 dpl, the lens appears substantially larger and occupies its original position in the middle anterior portion of the eye (Fig. 3F). At this point, 2°LFs are located on the periphery of the lens and assume a position surrounding the 1°LFs (Fig. 3F). It is known that as lens development takes place, LFs undergo autophagy and degrade their organelles to acquire transparency.<sup>42–44</sup> The difference in organelle composition between 1°LFs and 2°LFs gives the cells different scattering contrast, which can be differentiated in the enhanced-contrast inset OCT image (Fig. 3F). Although the regenerated lens has not reached the size of the original intact lens by 80 dpl, it has a mature and compact structure, with a thin anterior layer of LE, a defined nucleus filled with 1°LFs, and a developed cortex filled with 2°LFs.

### In Vivo Monitoring of Lens Regeneration From the Same Animal

With the *in vivo* imaging capability of OCT, we can observe the process of lens regeneration by tracking the same eye in an individual newt. To avoid stressing the animal with constant anesthesia, we took images sporadically for a period of 60 dpl. The sequence of morphological changes during lens regeneration recorded by OCT are shown in Figure 4. Although

some of the observations have been discussed in the last section, this approach demonstrates the feasibility of monitoring the morphological changes during regeneration from the same eye, thus producing more consistent results.

Immediately after lens removal, the incision made in the cornea was visible, and the iris was stretched toward the cornea as a result of the surgery (Fig. 4B). One of the most noticeable observations at 0 dpl was the dilation of blood vessels in the stroma of the iris (Fig. 4B). After taking a closer look at the blood vessels in the stroma of the dorsal iris at 0 dpl, we were able to capture the migration of cells inside the blood vessels (Supplementary Fig. S2 and Supplementary Movie S1). At 0 dpl, the space in the anterior chamber between the iris and the cornea was reduced compared with that of the intact eye (Fig. 4A, B). This was due to the corneal incision, which leads to leakage of aqueous humor, reducing the pressure in the anterior chamber of the eye and resulting in a partial collapse. At 5 dpl, the corneal wound is in the process of healing while ECM accumulates in the anterior chamber. Bright spots were observed within the ECM, suggesting that these are migrating cells recruited to the site of injury (Figs. 4C–H). These migrating cells were also seen in H&E images, indicating that they are not imaging artifacts (Figs. 3B'–D'). At 18 dpl, a lens vesicle (LV) was present at the pupillary margin of the Di, and the ECM levels were reduced (Fig. 4F). As the LE at the anterior surface of the lens continued to proliferate and differentiate into LFs, the lens volume increased (Figs. 4H–O). At this stage, the visible migrating cells in the anterior chamber started to gradually decrease in number and continued to decrease during the late stages of lens regeneration (Figs. 4I–O). By 25 dpl, the regenerating lens assumed a spherical shape, with the lens fibers arranged in concentric spherical shells (Figs. 4H–O). The distance between the cornea and the iris in the anterior chamber was increased to a similar level to the intact eye by 60 dpl as the newly developed aqueous chamber covered the anterior part of the eye (Figs. 4A, O).

### 3D View of the Lens Regeneration

To gain a more detailed, multi-angle view of lens regeneration, we reconstructed 3D images from the OCT B-scans. We performed 3D reconstructions of the intact eye and at different stages during lens regeneration (Fig. 5, Supplementary Fig. S3, Supplementary Movie S2). These 3D images were reconstructed from B-scans collected from both studies and are, therefore, not from the same animal. Different tissues were marked with independent pseudo-color channels, with

the iris in blue, the cornea in green, and the lens in red. In the uninjured eye, the intact lens covered the entire pupillary margin (Fig. 5A, Supplementary Fig. S3A). After lensectomy, the area between the iris and cornea collapsed due to leakage of the aqueous chamber (Figs. 5B, C; Supplementary Fig. S3B, C). During the early stages of lens regeneration, the lens initiated from the Di and appeared as an irregular elliptical vesicle (Figs. 5D–F; Supplementary Figures S3D–F, Fig. S4), which gradually grew to a more spherical shape as it increased in size (Figs. 5G–I, Supplementary Fig. S3G–I).

Acquisition of 3D images allowed us to quantify the change in lens volume during regeneration. Lens volume was quantified by measuring lens growth from the same eye of an individual newt (Fig. 4) from 18 dpl until 60 dpl. The regenerated lens volume displayed a quadratic correlation with days post-lensectomy, defined as  $V(t)$ . The regenerating lens growth rate,  $R(t)$ , was estimated by calculating the derivative of the  $V(t)$ , which showed an increasing linear relationship with days post-lensectomy, and it increased continually until 60 dpl (Fig. 6).

## Discussion

In the present study, we describe the use of OCT to track the process of newt lens regeneration *in vivo* for the first time, to the best of our knowledge, since Colucci and Wolff originally described this process in the 1890s.<sup>45,46</sup> We compared OCT-acquired images of newt lens regeneration to corresponding H&E images using a total of 36 animals. We also demonstrated that OCT can be used to capture images of the lens regeneration process from the same eye of an individual newt continuously for 60 dpl. Using OCT 3D volumetric imaging, we were able to quantify the change in lens volume during regeneration and view the 3D spatial relationship among the lens, iris, and peripheral structures.

By comparing OCT images of newt lens regeneration obtained from live animals to the corresponding H&E images of collected eyes, we demonstrated that OCT is able to capture the most important morphological features shown in the H&E images. The cornea, iris, and regenerated lens (including LE and the LFs) can be identified by OCT and confirmed by H&E staining. Because the OCT images were obtained *in vivo*, the native architecture of the eye was preserved, whereas with H&E processing unwanted artifacts including tissue tearing, shrinking, and flattening can be introduced.<sup>47</sup>

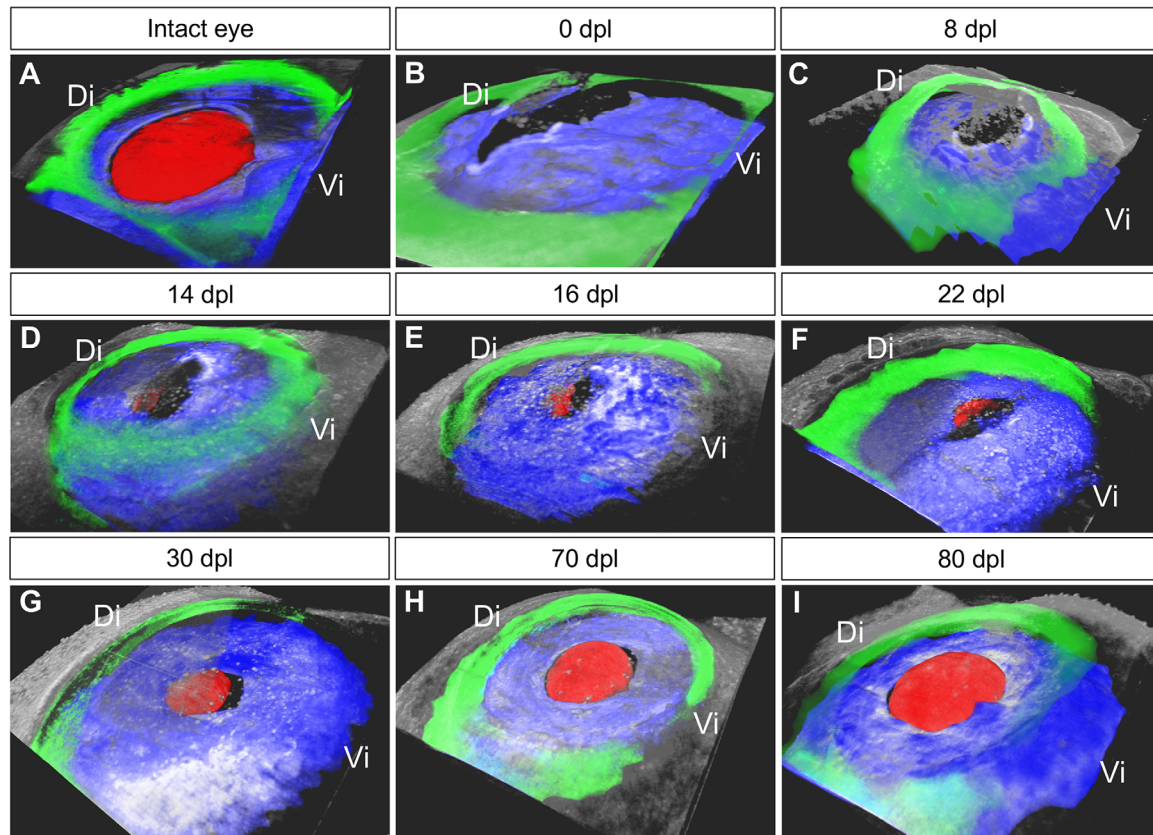


**Figure 5.** C-scan 3D reconstruction of newt eyes during lens regeneration (anterior view). The intact lens occupies the entire pupillary area (A). After lens removal at 0 and 8 dpl, the fluid of the aqueous chamber leaks out of the open cornea, and the space between the iris and cornea collapses (B, C). A LV is visible at 14 dpl at the pupillary margin of the mid-Di and with an irregular elliptical shape (D). At 16 and 22 dpl, the LV grows and occupies more space at the pupillary margin (E, F). At 30 dpl, the regenerating lens assumes a spherical shape (G). At later stages, the regenerating lens keeps growing in size as lens fibers differentiate and eventually occupy the entire pupillary area (G–I). The eye orientation is kept the same in all images, with Di on the left and Vi on the right. The multi-channels stack consist of four single-color channels with 8-bit intensity (255 intensity levels for each channel). The opacity levels (0–1) of the green, blue, and red channels are adjusted between 0.4 and 0.9 so that the OCT image grayscale signal can still be visible through color channels. The gray channel intensity was sharpened to increase the contrast, and the range is between 40 and 250. C-scan volume:  $1.2 \times 1.2 \times 1.35 \text{ mm}^3$ .  $\text{mm}^3$  3D visualization is available in Supplementary Movie S2. Blue, iPECs; red, regenerating lens; green: cornea.

The non-invasive aspect of OCT also allows minimizing animal usage. Mechanistic studies of regeneration often rely on the administration of chemicals to impact the overall regenerative process.<sup>48–53</sup> Unlike the case with limb or tail regeneration, lens regeneration takes place inside the eye, hidden from view. In the past, large numbers of animals were required to observe the impact of chemicals in the entire process of lens regeneration. OCT provides a way to circumvent this issue and validate large numbers of agents capable of inducing or inhibiting regeneration with a minimal number of animals per treatment. One of the most spectacular aspects of newt lens regeneration is the fact that, in contrast to the Di, the morphologically identical PECs of the Vi are incapable of regenerating a lens *in vivo*. OCT provides an excellent opportunity to perform comparative studies to investigate signaling

pathways between regeneration-competent and incompetent tissues. We have shown that OCT can detect LVs from the Di as early as 14 dpl. It is feasible to employ OCT to conduct future studies to identify agents capable of inducing lens regeneration from the ventral iris with a smaller cohort of animals than those required in traditional studies.

OCT can acquire thousands of *in vivo* 3D images in a few seconds, whereas H&E images require extensive work for a few sectional images. With 3D images, we are able to view the spatial relationship between the lens and the iris and quantify the volumetric changes during lens regeneration. It has been known for a long time that the regenerated lens is initiated from transdifferentiated iPECs. However, from the OCT 3D images we are now able to show that the initial regenerating lens vesicle and lens do not develop as a sphere from

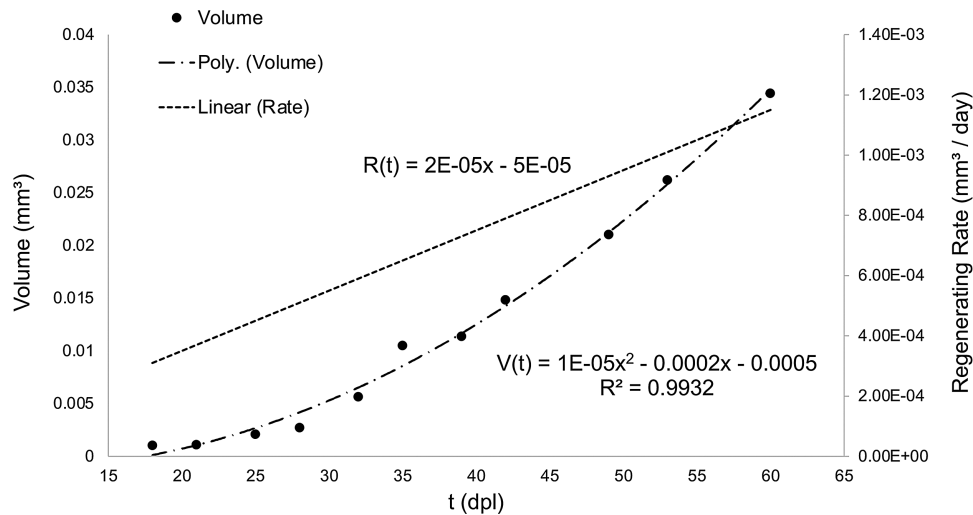


**Figure 6.** Quantification of lens growth during regeneration. The volume of the regenerating lens from a single animal was quantified by calculating the lens volume,  $V(t)$ , using the methods described in Figure 2. The regenerating lens volume was measured at 11 different time points over the course of 60 days. The regenerating rate,  $R(t)$ , represents the derivative of  $V(t)$  with respect to days post-lentectomy (dpl), measuring the lens growth rate at each dpl.  $V(t)$  shows that the regenerating lens volume has a quadratic relationship with dpl, whereas the  $R(t)$  indicates the regenerating growth rate of the lens has a linear relationship with dpl.

the pupillary mid-Di margin but instead extends along the Di as an elliptical structure, which likely supports the involvement of more PECs in the regeneration process (Supplementary Fig. S4). By quantifying the volume of the regenerated lens, we were able to determine that the lens volume increased linearly with days post-lentectomy. Although we do not have data beyond 60 dpl, it can be expected that the growth rate of the lens will eventually decrease as the regenerating lens approaches the size of the lens prior to removal.

With OCT imaging, we can not only identify the blood vessels in the stroma but also monitor the movement of circulating cells within these vessels. Our observations suggest that these blood vessels become dilated (vasodilation) immediately after injury and during the early stages of lens regeneration. The significance of blood vessel dilation during the lens regeneration process is not known. However, it was recently shown that circulating erythrocytes play an important role in limb regeneration by providing secretory molecules such as growth factors and matrix metalloproteases at the site of injury.<sup>54</sup> Whether circulating erythrocytes play a similar role during lens regeneration remains to be explored. Even though previous whole-mount fluorescent imaging demonstrated that the distribution of blood vessels between dorsal and ventral iris is similar,<sup>55</sup> OCT may allow us to quantify the dilation of the blood vessels and blood flow rates or oxygen saturation levels to uncover the function and contribution of these biological processes during dorsal iPec transdifferentiation.

Additionally, we have shown that OCT can capture the accumulation and clearance of ECM in the aqueous chamber during regeneration. Previous studies have demonstrated the importance of ECM during limb regeneration in newts.<sup>56</sup> ECM accumulation seems concurrent with the appearance of migrating cells, especially before and during LV formation (0–14 dpl). Several studies in axolotls, a closely related species, suggest a potential interplay between immune cells and ECM remodeling to promote scar-free healing in these regeneration-competent animals.<sup>57–59</sup> Therefore, our observations lead us to speculate that ECM might serve as a scaffold for immune cells and other cell types to migrate to the injury site. It will be interesting in the future to use OCT to explore in real time the potential crosstalk between ECM and immune cells. Indeed, several reports document the ability of OCT technology to image and quantify ECM remodeling and immune cell activity.<sup>60,61</sup>

There are several limitations to the present study. The OCT system at ~850 nm used here has a limited coherent length of ~4 mm which prevents us from capturing the entire regenerated lens after ~49 dpl. By employing swept-source OCT at ~1000 nm, which has a much longer coherence length and deeper imaging depth, we may be able to capture the regenerated lens at later stages.<sup>62,63</sup> At the early stages of lens regeneration, our current OCT setup can capture the LV and ECM, but the scattering contrast from them is low. To better visualize them, it is possible to image the lens regeneration process at the early stages with

OCT in the visible light range, which can provide better contrast and resolution.<sup>64</sup> Mapping blood flow rates during regeneration may provide new dynamic insight into lens regeneration. We have noticed our current frame rate of 17 frames/s is insufficient to quantify the blood flow rate in the iris stroma. We expect to significantly improve the imaging speed to above ~100 frames/s for future studies. Finally, we only tracked a single eye for quantifying the volumetric and lens growth rate relationship with days post-lentectomy. We expect to track a larger sample size with an improved OCT system in the future.

## Conclusions

We have established OCT as a powerful and reliable imaging modality for monitoring *in vivo* the process of newt lens regeneration. Compared with traditional *ex vivo* imaging technologies, OCT opens the door to track lens regeneration dynamics on the same eye repeatedly, making our observations more consistent, and free from tissue processing artifacts. Additionally, 3D OCT images give us a new perspective by capturing the spatial relationships during the process of lens regeneration, which may shed new mechanistic insights into this process. Elucidating the mechanisms of lens regeneration will provide clues for unlocking the regenerative potential of higher vertebrates and for developing therapies to treat or prevent blinding disorders in humans.

## Acknowledgments

In loving memory of Panagiotis A. Tsonis. The authors thank Miami University Laboratory Animal Resources staff and director for maintaining and monitoring all animals involved in this study. The authors thank Michael L. Robinson, Raul Perez Estrada, Erika Grajales-Esquivel, Tracy Haynes, Arielle Martinez, and Alyssa Miller for critical reading of the manuscript.

Supported by Grants from the National Eye Institute (RO1 EY027801 to KDRT; R21 EY031865 to HW and KDRT), and Miami University Doctoral Undergraduate Opportunity Scholarships to GT and JC.

Disclosure: **W. Chen**, None; **G. Tsissios**, None; **A. Sallese**, None; **B. Smucker**, None; **A.-T. Nguyen**, None; **J. Chen**, None; **H. Wang**, None; **K. Del Rio-Tsonis**, None

\* WC and GT had equal contribution as 1st authors.

## References

1. Henry JJ, Tsonis PA. Molecular and cellular aspects of amphibian lens regeneration. *Prog Retin Eye Res.* 2010;29(6):543–555.
2. Henry JJ. The cellular and molecular bases of vertebrate lens regeneration. *Int Rev Cytol.* 2003;228:195–265.
3. Sousounis K, Athipposhy AT, Voss SR, Tsonis PA. Plasticity for axolotl lens regeneration is associated with age-related changes in gene expression. *Regeneration (Oxf).* 2014;1(3):47–57.
4. Suetsugu-Maki R, Maki N, Nakamura K, et al. Lens regeneration in axolotl: new evidence of developmental plasticity. *BMC Biol.* 2012;10:103.
5. Vergara MN, Tsissios G, Del Rio-Tsonis K. Lens regeneration: a historical perspective. *Int J Dev Biol.* 2018;62(6–8):351–361.
6. Eguchi G, Eguchi Y, Nakamura K, Yadav MC, Millán JL, Tsonis PA. Regenerative capacity in newts is not altered by repeated regeneration and ageing. *Nat Commun.* 2011;2:384.
7. Sousounis K, Qi F, Yadav MC, et al. A robust transcriptional program in newts undergoing multiple events of lens regeneration throughout their lifespan. *eLife.* 2015;4:e09594.
8. Barbosa-Sabanero K, Hoffmann A, Judge C, Lightcap N, Tsonis PA, Del Rio-Tsonis K. Lens and retina regeneration: new perspectives from model organisms. *Biochem J.* 2012;447(3):321–334.
9. Del Rio-Tsonis K, Jung JC, Chiu IM, Tsonis PA. Conservation of fibroblast growth factor function in lens regeneration. *Proc Natl Acad Sci USA.* 1997;94(25):13701–13706.
10. Eguchi G. Electron microscopic studies on lens regeneration I. Mechanism of depigmentation of the iris. *Embryologia.* 1963;8:45–62.
11. Eguchi G. Electron microscopic studies on lens regeneration II. Formation and growth of lens vesicle and differentiation of lens fibers. *Embryologia.* 1964;8:247–287.
12. Yamada T. Control mechanisms in cell-type conversion in newt lens regeneration. *Monogr Dev Biol.* 1977;13:1–126.
13. Wassmer S, Beddaoui M, Rajai P, Munger R, Tsilfidis C. A focus on the optical properties of the regenerated newt lens. *PLoS One.* 2013;8(8):e70845.
14. Madhavan M, Haynes TL, Frisch NC, et al. The role of Pax-6 in lens regeneration. *Proc Natl Acad Sci USA.* 2006;103(40):14848–14853.
15. Grogg MW, Call MK, Okamoto M, Vergara MN, Del Rio-Tsonis K, Tsonis PA. BMP

- inhibition-driven regulation of six-3 underlies induction of newt lens regeneration. *Nature*. 2005;438(7069):858–862.
16. Huang D, Swanson EA, Lin CP, et al. Optical coherence tomography. *Science*. 1991;254:1178–1181.
  17. Jonnal RS, Kocaoglu OP, Zawadzki RJ, Liu Z, Miller DT, Werner JS. A review of adaptive optics optical coherence tomography: technical advances, scientific applications, and the future. *Invest Ophthalmol Vis Sci*. 2016;57(9):Oct51–Oct68.
  18. Hee MR, Izatt JA, Swanson EA, et al. Optical coherence tomography of the human retina. *Arch Ophthalmol*. 1995;113(3):325–332.
  19. Hirano K, Ito Y, Suzuki T, Kojima T, Kachi S, Miyake Y. Optical coherence tomography for the noninvasive evaluation of the cornea. *Cornea*. 2001;20(3):281–289.
  20. Huber G, Beck SC, Grimm C, et al. Spectral domain optical coherence tomography in mouse models of retinal degeneration. *Invest Ophthalmol Vis Sci*. 2009;50(12):5888–5895.
  21. Ruggeri M, Wehbe H, Jiao S, et al. In vivo three-dimensional high-resolution imaging of rodent retina with spectral-domain optical coherence tomography. *Invest Ophthalmol Vis Sci*. 2007;48(4):1808–1814.
  22. Li Q, Timmers AM, Hunter K, et al. Noninvasive imaging by optical coherence tomography to monitor retinal degeneration in the mouse. *Invest Ophthalmol Vis Sci*. 2001;42(12):2981–2989.
  23. Leung CK, Cheung CY, Weinreb RN, et al. Comparison of macular thickness measurements between time domain and spectral domain optical coherence tomography. *Invest Ophthalmol Vis Sci*. 2008;49(11):4893–4897.
  24. Huckenpahler AL, Lookfong NA, Warr E, Hefferman E, Carroll J, Collery RF. Noninvasive imaging of cone ablation and regeneration in zebrafish. *Transl Vis Sci Technol*. 2020;9(10):18.
  25. Weber A, Hochmann S, Cimalla P, et al. Characterization of light lesion paradigms and optical coherence tomography as tools to study adult retina regeneration in zebrafish. *PLoS One*. 2013;8(11):e80483.
  26. Zhou KJ, Li YN, Huang FR, Wang QM, Yu AY. In vivo observation of lens regeneration in rat using ultra-long scan depth optical coherence tomography. *Invest Ophthalmol Vis Sci*. 2016;57(15):6615–6623.
  27. Lin YS, Chu CC, Lin JJ, et al. Optical coherence tomography: a new strategy to image planarian regeneration. *Sci Rep*. 2014;4:6316.
  28. Bhavsar RB, Nakamura K, Tsonis PA. A system for culturing iris pigment epithelial cells to study lens regeneration in newt. *J Vis Exp*. 2011;52:2713.
  29. Simon HG, Odelberg S. Maintaining Eastern newts (*Notophthalmus viridescens*) for regeneration research. *Methods Mol Biol*. 2015;1290:17–25.
  30. Zhao Y, Wang H. Spectral calibration for spectral domain optical coherence tomography based on B-scan Doppler shift with tissue images. *J Opt*. 2019;21(9):095302.
  31. Eguchi G. Cellular and molecular background of wolffian lens regeneration. *Cell Differ Dev*. 1988;25(suppl):147–158.
  32. Tsonis PA, Madhavan M, Tancous EE, Del Rio-Tsonis K. A newt's eye view of lens regeneration. *Int J Dev Biol*. 2004;48(8–9):975–980.
  33. Sousounis K, Bhavsar R, Looso M, et al. Molecular signatures that correlate with induction of lens regeneration in newts: lessons from proteomic analysis. *Hum Genomics*. 2014;8(1):22.
  34. Sousounis K, Looso M, Maki N, Ivester CJ, Braun T, Tsonis PA. Transcriptome analysis of newt lens regeneration reveals distinct gradients in gene expression patterns. *PLoS One*. 2013;8(4):e61445.
  35. Eguchi G, Del Rio-Tsonis K. Lens regeneration. In: Lovicu FJ, Robinson ML, eds. *Development of the Ocular Lens*, Cambridge, UK: Cambridge University Press; 2004;290–311.
  36. Zhu J, Zhang E, Del Rio-Tsonis K. Eye anatomy. *eLS*. 2012;2012:1–9.
  37. Wilk MA, Huckenpahler AL, Collery RF, Link BA, Carroll J. The effect of retinal melanin on optical coherence tomography images. *Transl Vis Sci Technol*. 2017;6(2):8.
  38. Meleppat RK, Zhang P, Ju MJ, et al. Directional optical coherence tomography reveals melanin concentration-dependent scattering properties of retinal pigment epithelium. *J Biomed Opt*. 2019;24(6):1–10.
  39. Freddo TF. Ultrastructure of the iris. *Microsc Res Tech*. 1996;33(5):369–389.
  40. Hsiao A, Hunter M, Greiner C, Gupta S, Georgakoudi I. Noninvasive identification of subcellular organization and nuclear morphology features associated with leukemic cells using light-scattering spectroscopy. *J Biomed Opt*. 2011;16(3):037007.
  41. Kalashnikov M, Choi W, Yu CC, et al. Assessing light scattering of intracellular organelles in single intact living cells. *Opt Express*. 2009;17(22):19674–19681.
  42. Chaffee BR, Shang F, Chang ML, et al. Nuclear removal during terminal lens fiber cell differentiation requires CDK1 activity: appropriating

- mitosis-related nuclear disassembly. *Development*. 2014;141(17):3388–3398.
43. Cvekl A, Ashery-Padan R. The cellular and molecular mechanisms of vertebrate lens development. *Development*. 2014;141(23):4432–4447.
  44. Wride MA. Minireview: apoptosis as seen through a lens. *Apoptosis*. 2000;5(3):203–209.
  45. Colluci VL. *Sulla rigenerazione parziale dell' occhio nei Tritoni: istogenesi e sviluppo*. Bologna: Studio sperimentale; 1891:593–629.
  46. Wolff G. Entwicklungsphysiologische Studien. I. Die Regeneration der Urodelenlinse. *Arch Mikrosk Anat Entwickl Org*. 1895;1:380–390.
  47. Taqi SA, Sami SA, Sami LB, Zaki SA. A review of artifacts in histopathology. *J Oral Maxillofac Pathol*. 2018;22(2):279.
  48. Vincent E, Villiard E, Sader F, Dhakal S, Kwok BH, Roy S. BMP signaling is essential for sustaining proximo-distal progression in regenerating axolotl limbs. *Development*. 2020;147(14):dev170829.
  49. Ponomareva LV, Athipozhy A, Thorson JS, Voss SR. Using *Ambystoma mexicanum* (Mexican axolotl) embryos, chemical genetics, and microarray analysis to identify signaling pathways associated with tissue regeneration. *Comp Biochem Physiol C Toxicol Pharmacol*. 2015;178:128–135.
  50. Tsonis PA, Vergara MN, Spence JR, et al. A novel role of the hedgehog pathway in lens regeneration. *Dev Biol*. 2004;267(2):450–461.
  51. Del Rio-Tsonis K, Trombley MT, McMahon G, Tsonis PA. Regulation of lens regeneration by fibroblast growth factor receptor 1. *Dev Dyn*. 1998;213(1):140–146.
  52. Tsonis PA, Trombley MT, Rowland T, Chandraratna RA, del Rio-Tsonis K. Role of retinoic acid in lens regeneration. *Dev Dyn*. 2000;219(4):588–593.
  53. Tsonis PA, Washabaugh CH, Del Rio-Tsonis K. Morphogenetic effects of 9-*cis*-retinoic acid on the regenerating limbs of the axolotl. *Roux's Arch Dev Biol*. 1994;203(4):230–234.
  54. Casco-Robles RM, Watanabe A, Eto K, et al. Novel erythrocyte clumps revealed by an orphan gene *Newtic1* in circulating blood and regenerating limbs of the adult newt. *Sci Rep*. 2018;8(1):7455.
  55. Imokawa Y, Brockes JP. Selective activation of thrombin is a critical determinant for vertebrate lens regeneration. *Curr Biol*. 2003;13(10):877–881.
  56. Vinarsky V, Atkinson DL, Stevenson TJ, Keating MT, Odelberg SJ. Normal newt limb regeneration requires matrix metalloproteinase function. *Dev Biol*. 2005;279(1):86–98.
  57. Arenas Gómez CM, Sabin KZ, Echeverri K. Wound healing across the animal kingdom: crosstalk between the immune system and the extracellular matrix. *Dev Dyn*. 2020;249(7):834–846.
  58. Godwin JW, Pinto AR, Rosenthal NA. Macrophages are required for adult salamander limb regeneration. *Proc Natl Acad Sci*. 2013;110(23):9415–9420.
  59. Godwin JW, Debuque R, Salimova E, Rosenthal NA. Heart regeneration in the salamander relies on macrophage-mediated control of fibroblast activation and the extracellular landscape. *NPJ Regen Med*. 2017;2:22.
  60. Blackmon RL, Sandhu R, Chapman BS, et al. Imaging extracellular matrix remodeling in vitro by diffusion-sensitive optical coherence tomography. *Biophys J*. 2016;110(8):1858–1868.
  61. Tearney GJ, Yabushita H, Houser SL, et al. Quantification of macrophage content in atherosclerotic plaques by optical coherence tomography. *Circulation*. 2003;107(1):113–119.
  62. Potsaid B, Baumann B, Huang D, et al. Ultrahigh speed 1050nm swept source/Fourier domain OCT retinal and anterior segment imaging at 100,000 to 400,000 axial scans per second. *Opt Express*. 2010;18(19):20029–20048.
  63. Grulkowski I, Liu JJ, Potsaid B, et al. Retinal, anterior segment and full eye imaging using ultrahigh speed swept source OCT with vertical-cavity surface emitting lasers. *Biomed Opt Express*. 2012;3(11):2733–2751.
  64. Shu X, Beckmann L, Zhang H. Visible-light optical coherence tomography: a review. *J Biomed Opt*. 2017;22(12):1–14.

## Supplementary Material

Supplementary Movie S1. Migration of cells within blood vessels of the iris recorded at 0 dpl.

Supplementary Movie S2. 3D visualization of newt intact eye and at 0,8,14,16,22,30,60, 70 and 80 dpl  
Blue: iPECs; Red: Regenerating lens; Green: Cornea.